Computers and Electronics in Agriculture 205 (2023) 107591

Contents lists available at ScienceDirect

Computers and Electronics in Agriculture

journal homepage: www.elsevier.com/locate/compag

Original papers

Placement and drone flight path mapping of agricultural soil sensors using machine learning

Payton Goodrich [a,*], Omar Betancourt [a], Ana Claudia Arias [b], Tarek Zohdi [a]

[a] University of California Berkeley, Department of Mechanical Engineering, Berkeley, 94720, California, USA
[b] University of California Berkeley, Department of Electrical Engineering and Computer Science, Berkeley, 94720, California, USA

ARTICLE INFO

Keywords:
Agricultural sensors
UAVs
Genetic algorithms
Agent-based model
Geostatistics

ABSTRACT

Accurate soil data, which can be collected with agricultural sensors spaced at the half-variogram range, is crucial information for precision agriculture. Drones offer a unique advantage over other existing methods to sample data from soil sensors because of the high density of sensors required to gather spatially granular data to capture soil variability. To determine the placement of sensors within an agricultural field, a novel sequential gap-reduction algorithm that minimizes sensor overlap was developed and used to assign sensor placement for four types of agricultural fields. A genetic algorithm optimized multi-agent flight paths for scanning sensors in a simulated agricultural field using a robust agent-based model. The locations of soil sensors for a simulated 400 m center-pivot irrigation field were used to determine flight paths for swarms of 1-8 drones. Increasing the number of drones in the swarm had a negligible effect on total energy expenditure but reduced the time to scan the sensors from 19 min to less than three minutes. The proposed sequential gap reduction algorithm maximizes the coverage of any arbitrarily-shaped agricultural field with fewer sensors than a grid-based distribution in most cases. The proposed multi-agent flight path mapping can effectively and efficiently generate flight paths for variable numbers of drones to scan all sensors. The framework proposed here can be utilized and expanded for variable rate irrigation, precision application of biological control agents, and smart farming.

1. Introduction

Precision agriculture offers a pathway to increase crop yield while reducing water consumption, carbon footprint, and chemicals leaching into groundwater. Precision agriculture is the practice of collecting spatial and temporal data in an agricultural field to match the inputs to the site-specific conditions (Diacono et al., 2013). While industrial agriculture seeks to maximize crop yield, there is also the consideration of maintaining a healthy ecosystem. Fortunately, these are not competing interests; numerous case studies have demonstrated that adopting precision agriculture techniques increases crop yield while lessening detrimental environmental effects (Diacono et al., 2013; Ahrens et al., 2010; Sela et al., 2018). Consider first the use of irrigation in agriculture, which accounts for approximately 36.7% of the freshwater consumption in the U.S. (Dieter, 2018), 65% in China (Dalin et al., 2014), and 77% in New Zealand (Hedley and Yule, 2009). This is in part because crops need a large amount of water to grow. For example, high-production maize crops require 600,000 gallons of water per acre per season—about the same volume as an Olympic swimming pool (Comis, 2011). However, adopting precision agriculture practices such as variable-rate irrigation methods has proven to reduce water consumption by 26.3% (Hedley and Yule, 2009). Meanwhile, fixing nitrogen from the air to produce fertilizers is an extraordinarily energy-intensive process (Gellings and Parmenter, 2016) and accounts for nearly 2% of the U.S.'s annual CO_2 emissions (Ritchie and Roser, 2020). Crop plants recover only 30%–50% of nitrogen in fertilizers (Cassman et al., 2002), which means that over half of the nitrogen becomes a potential source of environmental pollution, such as groundwater contamination, eutrophication, acid rain, ammonia redeposition, and greenhouse gases (Ladha et al., 2005). Fortunately, precision agriculture practices have demonstrated an increase in nitrogen use efficiency (Ahrens et al., 2010; Gupta and Khosla, 2012), thereby reducing both the production volume of fertilizer and the amount that is polluted into the environment.

Accurate soil data is crucial information for precision agriculture (Robert et al., 1995). In particular, the moisture content (SU et al., 2014) and the concentration of various chemical analytes (Robertson et al., 1997; Shahandeh et al., 2005; Anthony et al., 2012) in soil have a significant influence on crop health and yield. These properties vary considerably over short distances, which begs the question: What spatial density does soil need to be sampled at to capture soil

* Corresponding author.
E-mail address: paytongoodrich@berkeley.edu (P. Goodrich).

https://doi.org/10.1016/j.compag.2022.107591
Received 21 June 2022; Received in revised form 16 December 2022; Accepted 21 December 2022
Available online 27 December 2022

variability? Half of the spatial range – referred to hereafter as the 'half-variogram range' (Bachmaier and Backes, 2008) – can be used as a "rule-of-thumb" to account for the spatial dependency of agricultural measurements (Kerry et al., 2010). The variance of a measurand, z, as a function of distance is empirically given by:

$$\hat{\gamma}(\vec{h}) = \frac{1}{2} \cdot \frac{1}{N(\vec{h})} \sum_{i=1}^{N(\vec{h})} \left[z\left(\vec{x}_i + \vec{h}\right) - z\left(\vec{x}_i\right) \right]^2 \quad (1)$$

where $\hat{\gamma}$ is the variance, $z\left(\vec{x}_i\right)$ and $z\left(\vec{x}_i + \vec{h}\right)$ are the measured values of the measurand z at $N(\vec{h})$ pairs of comparisons separated by the vector $\vec{h}$. Numerous studies have determined the spatial range of various soil properties in various soil conditions (Robertson et al., 1997; Shahandeh et al., 2005; Anthony et al., 2012; Kerry et al., 2010; Longchamps et al., 2015), which demonstrates the fact that the half-variogram range itself varies depending on the geographic location and sampling method (Kerry et al., 2010). Recently, Longchamps & Khosla analyzed and tabulated the spatial ranges of numerous soil properties reported in literature (Longchamps and Khosla, 2017), which can be used as informed estimates for spacing sensors when no other information about the soil is known.

Geostatistically representative soil data can be collected with agricultural sensors spaced at the half-variogram range (Kerry et al., 2010). The data gathered from these sensors can inform management techniques such as variable-rate technologies, which adapt to the heterogeneities of an agricultural field and thus enable site-specific management (Kanter et al., 2019; Evans, 2001; Evans et al., 2013; Lo et al., 2017). For example, farmers could tailor their nitrogen and water management to site-specific conditions (Finger et al., 2019), which would, in turn, reduce nitric oxide emissions, increase yields, and reduce fertilizer use (Ahrens et al., 2010). Other researchers have investigated the use of machine-learning algorithms as tools for decision-making in precision agriculture (Jourdan and de Weck, 2004; Chlingaryan et al., 2018; Akbarzadeh et al., 2014; Patrício and Rieder, 2018; Sun et al., 2022). However, to the best of our knowledge, no authors have optimized agricultural soil sensor placement using the half-variogram range to inform the placement of sensors.

Because many sensors need to be distributed across an agricultural field to acquire granular enough data to capture soil variability, drones offer a unique advantage over other existing methods to sample data from the sensors (Sørensen et al., 2017). With drones and drone accessories becoming less expensive, using multiple drones to simultaneously map sensors has become an attractive route to efficiently gather data (Tosato et al., 2019; Bertalan et al., 2022; Pereira et al., 2022). Machine-learning algorithms are a promising approach for generating flight path maps due to their ability to solve highly non-convex problems rapidly and even operate in real-time as a digital twin (Zohdi, 2021b,a, 2022).

This work develops a sequential gap reduction (SGR) algorithm that determines an optimal distribution of soil sensors across an agricultural field. The SGR algorithm is used to solve optimal sensor distribution using the half-variogram range as the basis in four field geometries: a circular field, a rectangular field, a field with both circular and rectangular features, and a field shape determined from an image. Finally, a methodology for sampling the sensor measurements using UAV swarms is proposed and characterized.

2. Theory

2.1. Digital expression of an agricultural field

Similar to how an agricultural field can be defined in the real world as a geographic area at a location, a digital representation – or 'simulation' – of an agricultural field can be defined as some number of discrete pixels, where each pixel's position corresponds to a geographic coordinate, and its size corresponds to an area. Three methods of expressing an agricultural field in a digital format are discussed.

For agricultural fields that a simple geometric shape can approximate – such as a rectangular field or a center-pivot irrigation field – expressing the farm digitally is trivial. For a rectangular-shaped field, the space is discretized into a grid of uniform pixels with dimensions proportional to the length and width of the physical field. For a center-pivot irrigation field, the field is bounded by a square grid of uniform pixels. Then, each pixel in the grid is tested to determine if the pixel's coordinates are equal to or less than the physical field radius. This technique is demonstrated in Fig. 1A for a rectangular-shaped field and Fig. 1B for a center-pivot irrigation field.

When the boundaries of the agricultural field are not regularly shaped, the field is defined by a list of consecutive coordinate points that form an enclosed shape when piecewise connected by polynomial curves. A ray tracing algorithm is adopted to determine whether or not a pixel is inside or outside of this boundary (Kumar and Bangi, 2018). Given an enclosed boundary and a point in space, if one were to draw an infinite vector in any direction originating from that point, it will intersect the boundary an odd-numbered amount of times if-and-only-if the point is within the enclosed space, which is shown in Fig. 1C. This holds for all points in space except for points on the boundary, which must be determined explicitly. This way, the coordinates of each pixel are used as a point to determine if a pixel is inside the boundary and append it to a list. A more detailed explanation of this method is described in the Supplementary Material.

Finally, satellite or drone visible-spectra images of agricultural land are already stored in a digital, pixelized format. Such images and datasets are widely available from Google Earth, NASA Earth Observatory, or the USDA cropland data layer, to name a few. Computer vision techniques can differentiate the arable land on a field from obstructions (such as roads, buildings, trees, and ponds) and store those pixels in a list (TOMBE, 2020; Akbari et al., 2021). This process is shown in Fig. 1D.

In all cases, it is important to note the physical dimensions that a single pixel represents. It should also be noted that because each method requires discretization of the field, the results are approximations whose accuracy increases proportionally to the number of pixels used.

2.2. Optimized sensor placement

The optimal layout of sensors in an agricultural field is achieved when, using the fewest number of sensors possible, all points in the field are statistically represented by the data collected by sensors in that field. For a given sensor, the data collected from that sensor is statistically significant for all points within a radial distance equal to the half-variogram range of that sensor (Kerry et al., 2010). Thus, if one considers an agricultural field as a two-dimensional collection of pixels described previously, one can model sensors as circles with a radius equal to the half-variogram range. Using this definition for optimal sensor placement, the problem is similar to the circle packing problem. Circle packing (or more broadly, "object packing") is a well-researched area in mathematics that has many practical applications (Hifi and M'hallah, 2009). Object packing aims to fit as many of some objects within a domain as possible without any overlap between the objects. There are several algorithms that aim to optimize object packing, such as random sequential addition (Widom, 1966), the Metropolis algorithm (Metropolis et al., 1953), and various particle growth schemes (Donev et al., 2005a,b). The limit of packing efficiency for equal-size circles in two dimensions is about 91% for a hexagonal grid (Steinhaus, 1999). While circle-packing nearly describes the model problem, there is one major caveat: no physical justification prevents the circles (sensors) from overlapping. This 'soft boundary' makes it possible to achieve 100% coverage of the domain by allowing overlap. If the only objective was to maximize the effective areal coverage of

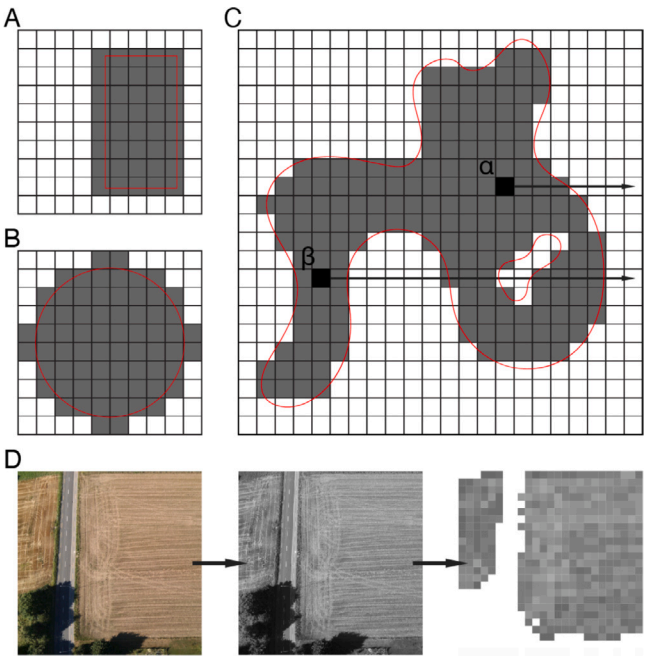

Fig. 1. Methods of defining agricultural fields in a digital domain. (A) Rectangular fields were defined by discretizing the field into a grid of uniform pixels proportional to the length and width of the physical field. (B) Center-pivot irrigation fields were defined by superimposing a uniform grid of pixels over the field and appending all pixels whose coordinates are within the radius of the pivot arm to a list of field pixels. (C) Irregularly shaped fields were defined by superimposing a uniform grid over the field and appending all pixels whose rays pass through an odd number of boundary lines. In this case, pixel α has a ray that passes through a single boundary line, while pixel β has a ray that passes through five boundary lines. (D) Digital images of agricultural fields are in a digital domain by definition but require computer vision techniques to determine which pixels in the image correspond to arable land.

the field, then one could simply distribute sensors next to one another without discretion. However, the monetary cost of sensors, sensor operation, and sensor maintenance makes this approach unreasonable, which motivates the stated objective of maximizing field coverage with the fewest sensors possible.

The SGR algorithm was developed and applied to place sensors within the field to minimize the overlap of each sensor's coverage radius. The general process is as follows:

1. **INITIALIZE:** Select a random pixel in the field and place a sensor there
2. **GENERATE:** Select a random pixel in the field
3. **TEST:** Check to see if a sensor placed at that pixel would overlap with any other sensor already placed in the field. If not, append that pixel to the list of placed sensors within the field.
4. **SCORE:** Compute the score of the design.
5. **ITERATE:** If the score is below the threshold, iterate through the algorithm.

The outcome of this algorithm is that sensors are placed throughout the field such that sensors are placed in the largest gaps between sensors. This is done by incrementing the acceptable distance between sensors by a small amount, then making many attempts at placing a sensor before repeating the process. The fitness of each placement design was scored by the ratio of the number of field pixels within the half-variogram range of a sensor to the total number of pixels in the field. In other words, what percentage of the field area is within the half-variogram range of one or more sensors? This process is repeated until it is impossible to place a sensor outside the range of all other sensors in the design, or until the field is completely covered. The flowchart for this algorithm is shown in Fig. 2A, and a schematic depicting the evolution of sensor placement in an arbitrary field shape is shown in Fig. 2B.

2.3. Data sampling

To make informed decisions about allocating resources for treating the soil, one must sample or collect the soil sensor data periodically throughout the growing season. When deployed, soil sensors are partially or completely buried under the soil using common farming equipment such as post augers or portable excavators. Depending on the design of the sensor, there are several ways that the data might be communicated. One method would be through a hardwire connection, such as a USB or Serial cable. An underground cable network would interfere with regular farming activities, but the sensors could be sampled by temporary connecting through a data port. However, this would require a data-reading device to come into direct contact with the sensor and a moderate level of precision to plug into the port. A simpler data transfer solution is integrating a transceiver into the sensor and transmitting the data wirelessly using RFID, Bluetooth Low Energy (BLE), Wi-Fi, or similar technologies. In this case, the data-reading device would only need to be within the transmission radius of the sensor to sample the sensor data. Generally speaking, the cost and complexity of the sensor increase dramatically as the transmission radius increases. For the technology to be practical for agricultural field operations, the associated costs of the sensor need to be minimal, so short-range transmission technologies are more feasible at scale (Deng et al., 2020).

There are several options one can choose to sample the sensor data. One option is using ground machinery (e.g. tractors) fitted with readers to receive sensor data as it traverses above them. Tractors are well suited to traverse through muddy or uneven ground, however, they can become costly as the fuel economy of such ground machinery can be poor. For a typical Fendt 1050 tractor model, the diesel consumption can be eight gallons per hour, and covering a large agricultural field may take the majority of a day (Hoy, 2021). This is not to mention the cost of a manned operator. A much more attractive option would be to incorporate unmanned vehicles, such as unmanned aerial vehicles (UAVs) or unmanned ground vehicles (UGVs). Unmanned vehicles typically have lower energy consumption than typical ground farm machinery and, as the name suggests, operate remotely, minimizing labor and operational costs. There are important distinctions to make between deploying ground-based and air-based vehicles. UGVs can typically withstand a larger range of weather conditions than UAVs but are limited to driving along the field rows to avoid damaging the crops. On the other hand, UAVs can traverse directly from sensor to sensor above the crop canopy. Because the energy consumption of small UAVs and UGVs are similar, the ability to traverse freely throughout a field makes UAVs more energy-efficient than UGVs. Assuming the soil sensors have a wireless transceiver integrated, the UAVs can sample data from the sensor from anywhere within the transmission radius, meaning the UAVs' positioning around the sensor does not have to be precise, and slight perturbations to the UAVs' position caused by weather will have a minor effect on the overall performance.

It is possible that a coordinated effort of multiple drones can further reduce the time and energy required to sample data from each sensor in the field. Furthermore, it may be difficult for a single UAV to scan all sensors due to battery life limitations. For these reasons, a flight path optimization model was developed for single-drone and multi-drone swarms to investigate their trade-offs.

2.4. Flight path mapping

A robust agent-based model was developed that generates flight paths for each drone within a swarm to scan all sensors within a simulated agriculture field. The simulations determine each drone's aerial route for optimal flight path planning (Zohdi, 2019; Mueller

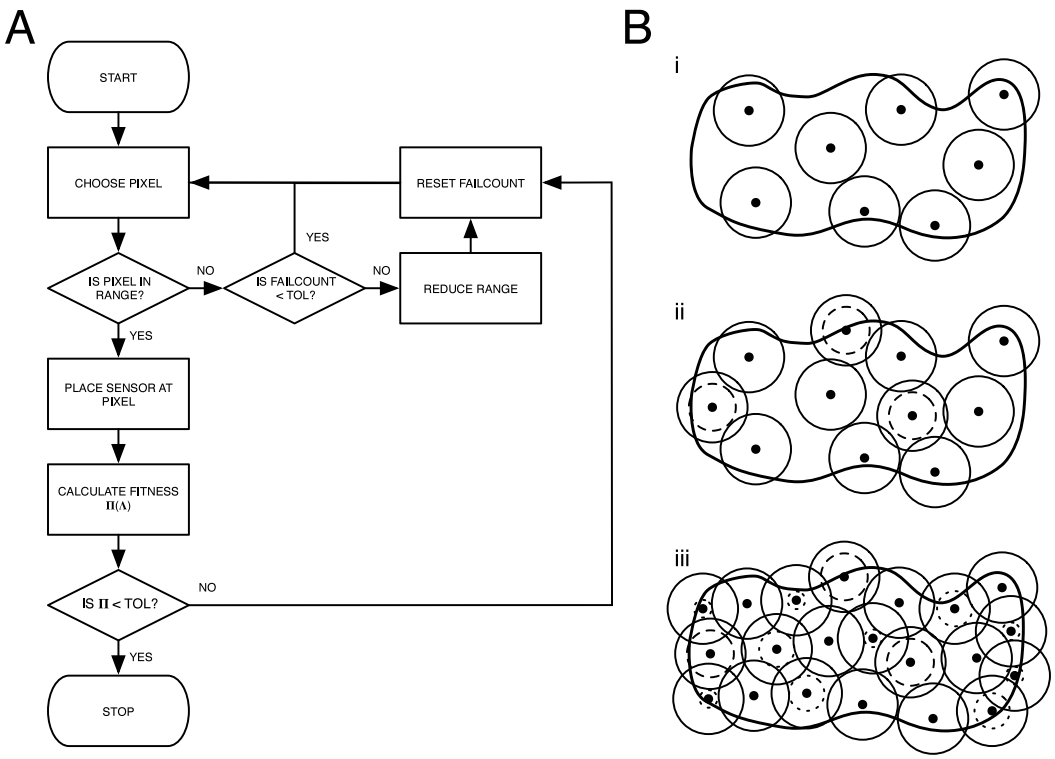

Fig. 2. (A) Flowchart of the Sequential Gap Reduction algorithm used to place sensors in a digitized agricultural field. (B) Schematic depicting the action of the Sequential Gap Reduction algorithm. (i) First, sensors are added to the field at randomly selected pixels within the field boundary such that there is no overlap between the sensors' effective coverage radius. The sensors are depicted as small black circles, and the sensor's effective coverage area is depicted as a solid line encircling the sensor. (ii) Once it is no longer possible to add any more sensors this way, the allowable minimum distance between sensors is decreased – represented by a dashed circle – while the effective coverage area of the sensors remains the same. (iii) This process is repeated until all gaps have been filled and all pixels within the boundary are within the effective coverage radius of at least one sensor.

et al., 2015). Each drone within the simulated framework, referred to as an 'agent', has unique characteristics that determine how it interacts with its surroundings, such as its environment and other drones. These characteristic parameters take inspiration from the physics of molecular dynamics, where each agent is modeled as a point-mass particle that is attracted and repelled by other objects within the system (Zohdi, 2021b). The framework inputs are the field's shape, the number of agents, and the sensor locations (targets). Depending on the field geometry and the locations of sensors within that field, the framework will output several suggestions of each drone's trajectory. Agents follow the simplified assumptions:

- The effects of buoyancy, lift, drag, and gravity are of secondary importance and may be neglected.
- The agents may propel themselves in any direction in 3D space.
- The agents may be idealized as point masses.
- The agents know the locations of all targets, obstacles, and other agents.

This framework is modeled in a fixed Cartesian basis in $\boldsymbol{e}_1$, $\boldsymbol{e}_2$, and $\boldsymbol{e}_3$ where the position $\boldsymbol{r}$, velocity $\boldsymbol{v}$ and acceleration $\boldsymbol{a}$ of a drone are described as:

$$\begin{aligned}\boldsymbol{r} &= r_1\boldsymbol{e}_1 + r_2\boldsymbol{e}_2 + r_3\boldsymbol{e}_3,\\ \boldsymbol{v} &= \dot{\boldsymbol{r}} = \dot{r}_1\boldsymbol{e}_1 + \dot{r}_2\boldsymbol{e}_2 + \dot{r}_3\boldsymbol{e}_3,\\ \boldsymbol{a} &= \ddot{\boldsymbol{r}} = \ddot{r}_1\boldsymbol{e}_1 + \ddot{r}_2\boldsymbol{e}_2 + \ddot{r}_3\boldsymbol{e}_3\end{aligned} \tag{2}$$

respectively. A schematic of this framework is shown in Fig. 3A.

The only force, F, imposed on each agent, i, is the agent's propulsion, which is assumed to be of constant magnitude. Hence each agent's equation of motion is described using Newton's second law:

$$m_i\boldsymbol{a}_i = \boldsymbol{F}_{p,i} = F\boldsymbol{n}_i^{\star}. \tag{3}$$

where m_i is the agent's mass, a_i is the agent's acceleration, and $\boldsymbol{n}_i^{\star}$ is the agent's propulsion vector.

The distance between an agent and other agents or sensors (hereafter referred to as 'objects') is imperative to calculate the propulsion's vector $\boldsymbol{n}_i^{\star}$. At each time step, the model calculates the Euclidean distance between objects, defined between agent i with position $\boldsymbol{r}_i$ and another object j in the system at $\boldsymbol{A}_j$, as:

$$d_{ij} \overset{\text{def}}{=} \|\boldsymbol{r}_i - \boldsymbol{A}_j\| = \sqrt{(r_{i1} - A_{j1})^2 + (r_{i2} - A_{j2})^2 + (r_{i3} - A_{j3})^2}. \tag{4}$$

The distance between an agent and other objects influences the magnitude of the attraction or repulsion force it has towards that particular object; Distant objects should have a weaker influence than near objects. Therefore, an exponentially decaying function is used to calculate the interaction vector between an agent and an object:

$$\hat{\boldsymbol{n}}_{i\to j} = (\underbrace{w_{att}e^{-c_{att}d_{ij}}}_{attraction} - \underbrace{w_{rep}e^{-c_{rep}d_{ij}}}_{repulsion})\boldsymbol{n}_{i\to j}. \tag{5}$$

where w_{att} and c_{att} are the weight and exponential decay coefficients of the attraction term, and w_{rep} and c_{rep} are the weight and exponential decay coefficients of the repulsion term, respectively. $\hat{\boldsymbol{n}}_{i\to j}$ is calculated for each type of object within the system, therefore agents and sensors will have their own values associated with w_{att}, c_{att}, w_{rep} and c_{rep}. The direction $\boldsymbol{n}_{i\to j}$ is the unit normal vector in the direction of the object j relative to agent i and is given by:

$$\boldsymbol{n}_{i\to j} = \frac{\boldsymbol{A}_j - \boldsymbol{r}_i}{\|\boldsymbol{A}_j - \boldsymbol{r}_i\|}. \tag{6}$$

Generally, a larger attraction term relative to the repulsion term causes net propulsion towards sensor objects. The total interaction vector between agent i and all objects of a particular type is the sum of all their interaction vectors, such as those shown in Fig. 3B. For

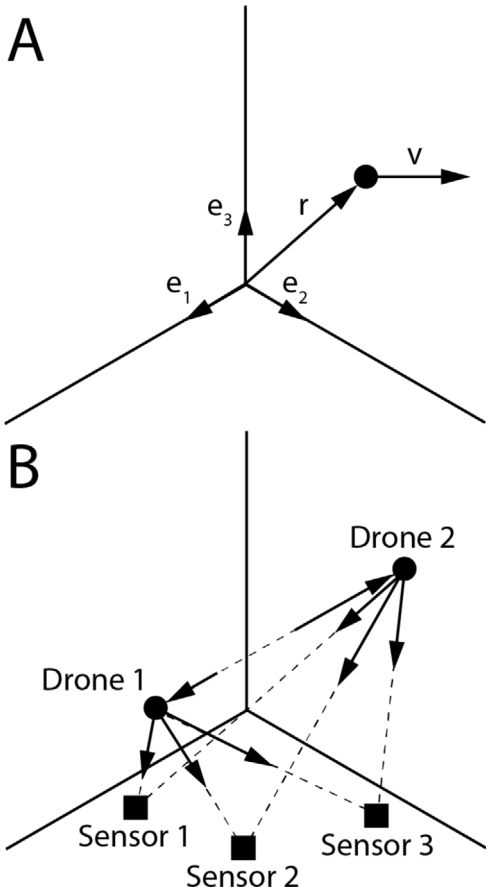

Fig. 3. (A) Schematic of a single-agent model in a Cartesian coordinate system. (B) Schematic of the interaction vectors in a two-agent, three-objective system. The instantaneous direction of drone acceleration will be in the net direction of the attraction and repulsion vectors acting on the drone, which changes in magnitude and direction as the drones move within the domain.

instance, the total interaction vector given by all sensors on agent i is:

$$\boldsymbol{N}_i^s = \sum_{j=1}^{N_{sensors}} \hat{\boldsymbol{n}}_{i\to j}^s \tag{7}$$

where $N_{sensors}$ is the total number of sensors in the system. A similar calculation is used for finding the interaction vector influenced by all other agents, $\boldsymbol{N}_i^a$. A weighted sum of the total interaction forces of sensors and agents is normalized to give the final direction of propulsion, i.e,

$$\boldsymbol{n}_i^\star = \frac{W_s \boldsymbol{N}_i^s + W_a \boldsymbol{N}_i^a}{\|W_s \boldsymbol{N}_i^s + W_a \boldsymbol{N}_i^a\|}. \tag{8}$$

Using this framework, the following algorithm determines the flight paths:

1. **INITIALIZE:** Load in the sensor location data within the simulated domain and position agents along one edge of the domain. Assign weight and exponential decay coefficients for each object's attraction and repulsion terms in Eq. (5).
2. **OBSERVE:** Each agent observes it's surroundings to calculate the attraction and repulsion terms and the optimal direction of propulsion as described in Eqs. (3)–(8).
3. **STEP:** Each agent will apply its thrust and accelerate toward the optimal direction.
4. **TEST:** If an agent is within the transmission range of a sensor, the sensor is considered scanned and removed from the domain. If an agent is within a 'crash radius' of another agent, both will be removed from the domain.
5. **ITERATE:** If there are unscanned sensors in the domain, iterate through the algorithm.

The magnitude and range of the interactive vectors between the agents and the targets were varied to optimize the flight paths, and the results were simulated. In this simulation, the number of mapped sensors were maximized while flight time and the number of collisions were minimized. Written as a cost function:

$$\Pi = W_1 \frac{N_{sensors} - N_{mapped}}{N_{sensors}} + W_2 \frac{t_{actual}}{t_{max}} + W_3 \frac{N_{crashed}}{N_{drones}} \tag{9}$$

where $N_{sensors}$ is the total number of sensors in the field, N_{mapped} is the number of sensors that were mapped by the drones, t_{actual} is the time it takes for the drones to map the sensors, t_{max} is the maximum allowed time for the mapping to take place, N_{drones} is the number of drones in the swarm, and $N_{crashed}$ is the number of drones that crashed into one another during the simulation. W_1, W_2, and W_3 are the user-defined weights given to each cost term.

A genetic algorithm was employed to minimize the cost function, using the magnitude and range of the interaction vectors as the design strings.

3. Computational model

3.1. Digital expression of an agricultural field

The two-dimensional problem for an agricultural field in a geographic coordinate system was encoded. First, the domain of the problem is expressed as $\bar{D}$, a $N_{dp} \times 2$ vector of values where N_{dp} is the number of pixels within the domain of consideration and the two columns are the longitudinal and latitudinal coordinates, respectively. Similarly, the agricultural field is expressed as $\bar{F}$, a $N_{fp} \times 2$ vector of values where N_{fp} is the number of pixels within the bounds of the field and the two columns are the longitudinal and latitudinal coordinates, respectively.

3.2. Optimized sensor placement

Sensor optimization throughout a field is achieved using the SGR algorithm. The algorithm is as follows:

1. **INITIALIZE:** For a given vector of field pixels, $\bar{F}$, select a random pixel within it and append it to $\bar{S}$, a $N_{sensors} \times 2$ vector of sensor coordinates, where $N_{sensors}$ is the number of sensors in the field.
2. **GENERATE:** Select a random pixel, $P = (p_x, p_y)$, within the field $\bar{F}$
3. **TEST:** For all S_i, where $S_i = (s_x, s_y)$, if $\|P - S_i\| \geq R_{hv}$, where R_{hv} is the half-variogram range of the sensor, then append P to $\bar{S}$
4. **SCORE:** Calculate fitness as the ratio of N_Γ to N_{fp}, where N_Γ is the number of pixels within distance R from any sensor pixel S_i: $\Pi(\Lambda) = \frac{N_\Gamma}{N_{fp}}$.
5. **ITERATE:** If $\Pi \leq TOL$, loop to Step 2.

The algorithm's speed can be further increased by incorporating a spatial hash. Spatial hashing is further discussed in the Supplementary Material.

3.3. Flight path mapping

The algorithm for optimizing the system parameters for flight paths for each drone is as follows:

1. **POPULATION GENERATION:** For a given number of drones, N_{drones}, randomly generate a population of G genetic strings, Λ^i, (i = 1,2, 3, …, G):

$$\Lambda^i \overset{\text{def}}{=} \{\lambda_1^i, \lambda_2^i, \lambda_3^i, \lambda_4^i, \dots, \lambda_G^i\} \overset{\text{def}}{=} \{\lambda_1, \lambda_2, \lambda_3, \dots, \lambda_G\}^i$$

$$\Lambda^i \overset{\text{def}}{=} \{w_{att}, w_{rep}, c_{att}, c_{rep}\}^i$$

2. **PERFORMANCE EVALUATION:** Compute fitness of each string, $\Pi(\Lambda^i)$, (i=1, …, G):

$$\Pi(\Lambda^i) \overset{\text{def}}{=} W_1 \frac{N_{sensors} - N_{mapped}}{N_{sensors}} + W_2 \frac{t_{actual}}{t_{max}} + W_3 \frac{N_{crashed}}{N_{drones}}$$

3. **RANK:** Rank each string based on their cost output Π, where Rank 1 is the best performing design string that produced the lowest cost and Rank G the worst performing string:

$$\Pi(\Lambda^i, i = 1, \dots, G)$$
$$\Pi(\Lambda^1) \leq \Pi(\Lambda^2) \leq \cdots \leq \Pi(\Lambda^G)$$

4. **MATE:** Mate design strings to produce offspring:

$$\Lambda^i \overset{\text{def}}{=} \Phi^{(1)}\Lambda^i + (1 - \Phi^{(1)})\Lambda^{i+1}$$

where $0 \leq \Phi \leq 1$

5. **GENE ELIMINATION:** Eliminate poorly performing genetic strings, keep top parents and generated offspring
6. **POPULATION REGENERATION:** Repeat the process with the new gene pool and new *random* genetic strings

This process is repeated until the performance of a genetic string, $\Pi(\Lambda^i)$, falls below the tolerance limit, indicating that the cost function has been minimized. The minimization of the cost function Π is guaranteed to be monotone with increasing generations if the parent strings are retained, i.e., $\Pi(\Lambda^{opt,I}) \geq \Pi(\Lambda^{opt,I+1})$, where $\Lambda^{opt,I+1}$ and $\Lambda^{opt,I}$ are the best genetic strings from generations $I + 1$ and I, respectively. If one does not retain the parents in the algorithm above, it is possible that inferior-performing offspring may replace superior parents. Thus, top parents were kept for the subsequent generation.

4. Simulation

Digital expressions of four types of agricultural fields were generated to show the flexibility and range of the SGR sensor placement method. First, a 50-ha circular field with a half-mile (400 m) radius was generated. Second, a rectangular-shaped 93-ha field was generated. Third, a 22-ha field with straight and curved boundaries was generated. Finally, a field from an image of pixels was generated. For all simulations, the pixel size was set to one square meter.

Next, for each field type, optimal sensor placement was found using the SGR algorithm with 40 m as the half-variogram range, which is a conservative value for soil nitrate (Longchamps and Khosla, 2017; Cao et al., 2012).

The optimized locations of soil sensors in a center-pivot irrigation field were then inserted into the agent-based model to determine flight paths for UAV drone swarms of varying sizes. The simulation parameters are shown in Table 1. In this simulation, the transmission radius of the sensors was assumed to be 2 m, corresponding to the transmission radius of an RFID tag, which has been shown recently in other agricultural monitoring applications (Deng et al., 2020; Hardin et al., 2022).

To test the hypothesis that a swarm of drones would outperform a single drone, the simulation was executed for swarm sizes of 1–8 drones.

5. Results and discussion

The placement of sensors determined by the SGR algorithm is shown in Fig. 4A–D. In Fig. 4A, the placement of sensors in a circular field with a 400 m radius – which is a common length for a center-pivot irrigation arm (Evans, 2001) – was determined. Fig. 4B shows the optimal placement of sensors for a rectangular farm field with dimensions corresponding to the average small-family U.S. farm (MacDonald et al., 2013). As of 2017, small family farms make up 89% of farms in the U.S. (Hellerstein and Vilorio, 2019). Fig. 4C demonstrates that the SGR algorithm could adapt and generate sensor placement for an arbitrary field shape defined by several boundary points. In Fig. 4D, the SGR algorithm distributed sensors in a field generated from a digital image. The sensors were efficiently placed such that they cover all of the pixels of the image while ignoring the islands of non-field pixels, such as those in the ‘a’ and ‘l’. In real-world applications, this image could be captured from satellite imagery, such as those available on Google Earth, ArcGIS, or other publicly available data sets.

A hexagonal-grid sensor distribution scheme is shown in Fig. 4E–H. Hexagonal packing is the most efficient packing method known to date, and circles can be packed in two dimensions to completely cover an area when staggered by a distance of $R\sqrt{3}$ in the x-direction and $\frac{3R}{2}$ in the y-direction.

The field coverage for varying numbers of sensors for the SGR and hexagonal-packing schemes are shown in Fig. 4I–L. The SGR algorithm outperformed the efficient hexagonal-grid distribution scheme when less than 95% of the field is covered for the circular and rectangular field types. In the case of total field coverage, however, the hexagonal-packing method could cover the entire field with fewer sensors. This is because the SGR algorithm prioritizes maximizing field coverage at each step, making it superior to other distribution schemes when the domain is sufficiently spacious. However, if the field shape is relatively simple and total coverage is needed, then the hexagonal-packing approach outperforms SGR because the entire field area can be covered with fewer sensors. Distributing sensors this way could have other benefits during field operations. Sensor distribution and maintenance would be simpler than the SGR placement approach, which requires a calibrated GPS and field map for the sensors’ initial placement and subsequent maintenance events. As the complexity of the field becomes high, however, the SGR algorithm becomes preferential to the hexagonal-packing method. The number of sensors required to cover the user-defined boundary type field shown in Fig. 4C and G was the same. For the field generated from an image in Fig. 4D and H, the SGR algorithm outperformed the hexagonal packing scheme for any number of sensors, as shown in Fig. 4L, and required only 52 sensors to completely cover the field compared to 59 for the hexagonal packing method.

To validate that UAVs operating with optimized flight paths are more energy efficient than a traditional sweeping method or a UGV, the paths for all three were simulated for a 400 m center pivot irrigation field with sensors distributed using the SGR algorithm, shown in Fig. 5. Fig. 5A shows the path for a UGV, which is constrained to traversing through the concentric crop rows to avoid damaging the growing crop. Row spacing varies, though it is typically around 0.5–0.75 m for corn and generally less for smaller row crops. Since this is less than the transmission radius of the sensors, the UGV does not have to traverse every row of the field. Instead, the effective row spacing was set to 4 m to minimize the number of concentric sweeps performed by the UGV, resulting in a 59.6 km path. If the sensors were paired with a stronger transceiver – such as a BLE or WiFi module – than the UGV would be able to skip more rows with each concentric sweep. However, the cost of such modules is inhibitive, and an economic analysis motivating the use of RFID is presented in the Supplementary Materials. Fig. 5B shows the flight path for a UAV scanning the sensors using a traditional sweeping method. Because of the short transmission radius, the UAV has to make tight turns to reach all of the sensors, making for a 63.9 km

Table 1
Flight path simulation parameters.

Symbol	Type	Units	Value	Description
R_{field}	Scalar	m	400	Radius of the center-pivot irrigation field
R_{hv}	Scalar	m	40	Half-variogram range
$R_{transmission}$	Scalar	m	2	Sensor transmission radius
N_{drones}	Scalar	None	1–8	Number of drones in the simulation
W_a	Scalar	None	[1, 10]	Search bounds of interaction weight for agents
W_s	Scalar	None	[1, 10]	Search bounds of interaction weight for sensors
w_{att}^-, w_{att}^+	Scalar	None	[0, 1]	Search bounds for attraction term weight coefficient
c_{att}^-, c_{att}^+	Scalar	None	[0, 1]	Search bounds for attraction term decay coefficient
w_{rep}^-, w_{rep}^+	Scalar	None	[0, 1]	Search bounds for repulsion term weight coefficient
c_{rep}^-, c_{rep}^+,	Scalar	None	[0, 1]	Search bounds for repulsion term decay coefficient
F	Scalar	N	100	Drone magnitude of propulsion force
m	Scalar	kg	5	Drone mass
v_{max}	Scalar	m/s	10	Drone max velocity
R_{crash}	Scalar	m	2	Crash radius
W_1	Scalar	None	0.6	Cost function weight associated with mapping sensors
W_2	Scalar	None	0.1	Cost function weight associated with mapping speed
W_3	Scalar	None	0.3	Cost function weight associated with crashed drones
TOL	Scalar	None	0.05	Cost tolerance for GA

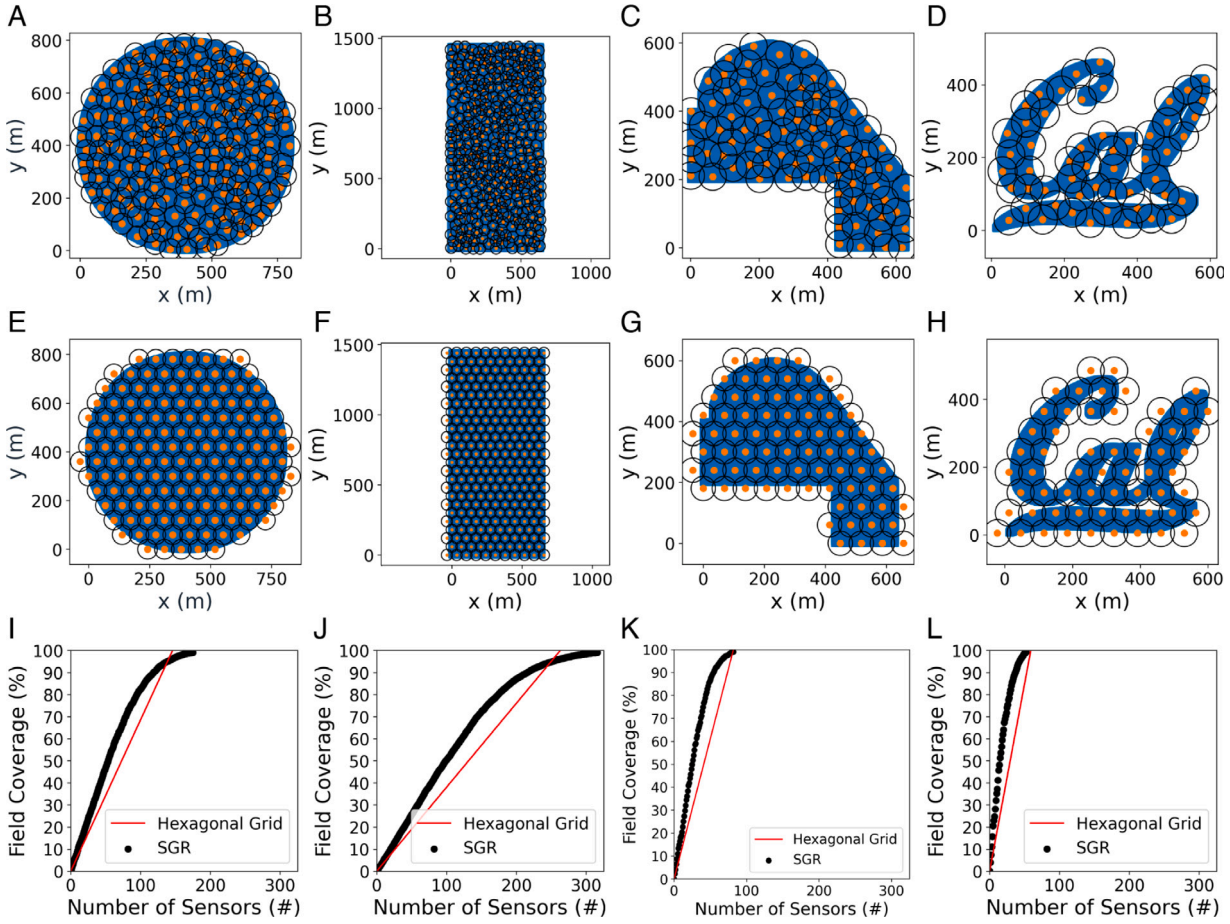

Fig. 4. Sensor placement using the (A–D) SGR algorithm and (E–H) hexagonal grid distributions using a 40 m half-variogram range as the effective sensing radius for various field types. The orange circular markers indicate the sensor coordinates, and the black ring around the sensor indicates the half-variogram range that the sensor covers. (A–D) Sensor placement for a circular field, rectangular field, user-defined boundary, and fields generated from an image using the SGR algorithm. (E–H) Sensor placement for a circular field, rectangular field, user-defined boundary, and fields generated from an image using a hexagonal grid spacing. (I–L) Plots of the effective field coverage for a given number of sensors corresponding to the field types above. The black curve is the field coverage for a distribution using the SGR algorithm, while the red line is for the hexagonal distribution.

flight path, which is even longer than the UGV. Finally, the optimized flight path for a single UAV is shown in Fig. 5C. When the agent-based optimization model is applied, the total path length is reduced to 11.4 km. While the agent-based method is more energy efficient than the traditional sweeping method, the comparison is more difficult to make against the case of UGVs, which consume power at a different rate than UAVs. The energy consumption of the three scenarios was calculated from the path lengths and the average power of the vehicles while neglecting the impact of start-stop behavior and turning. The total energy consumed to scan all of the sensors in the field was 165 kWh for UGVs, 0.32 kWh for UAVs performing a traditional sweep, and 0.06 kWh for UAVs with optimized flight paths.

To determine the ideal number of drones to use for sampling data from the distributed sensors, flight paths for swarms of n = 1–8

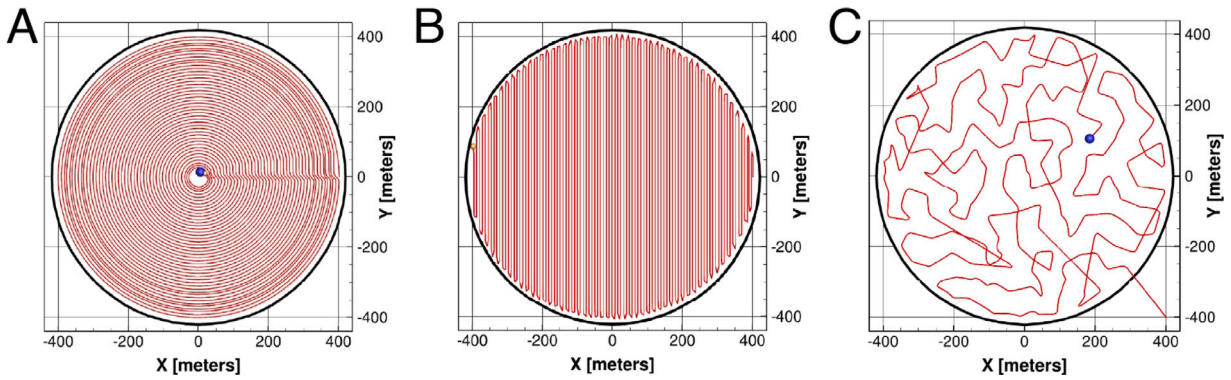

Fig. 5. Comparison of different data sampling strategies in a 400 m radius center-pivot irrigation field. (A) Manned or unmanned ground vehicles are restricted to traversing crop rows to prevent damaging the crops, which are radial in a center-pivot irrigation field. (B) A UAV performing a traditional sweep scan must execute tight sweeps to scan all the sensors. (C) A UAV with an optimized flight path has a significantly shorter path than the other sampling options making it the most energy efficient.

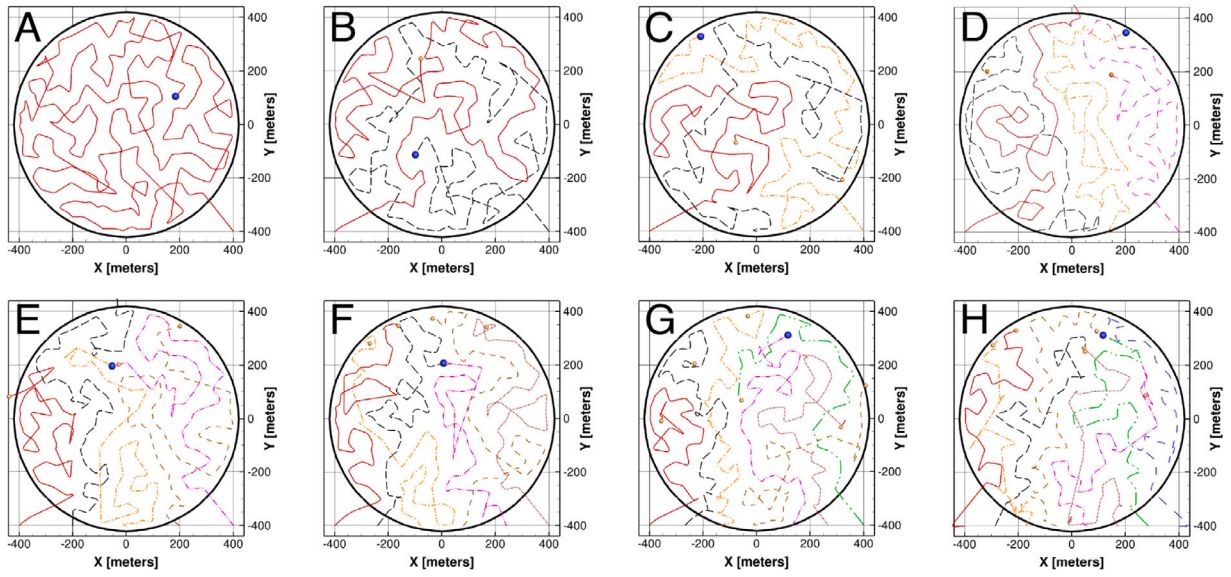

Fig. 6. Flight paths of drones scanning sensors in a 400 m radius center-pivot irrigation field for swarms of (A) 1, (B) 2, (C) 3, (D) 4, (E) 5, (F) 6, (G) 7, and (H) 8 agents, respectively.

drones were simulated. The optimized flight paths for the varying-sized swarms are shown in Fig. 6, and the total flight path length and flight time are shown in Fig. 7. Fig. 6A shows the flight path of a single agent. Fig. 6B and C show the flight paths for two and three agent swarms, respectively. In both cases, the agents frequently crossed each other's paths. As swarm size increases, such as for four agent swarms shown in Fig. 6D, the agents crossed paths less, and each agent subdivided the field into its own sections to scan the sensors within it, which is generally more efficient and less prone to accidental crashes in the event of interference or GPS malfunction. For swarms with five or more sensors, as shown in Fig. 6E–H, more overlapping occurred as agents began to compete over the same sensors. These results may also depend on each drone's initial starting position. The agents in this example were placed at the edge and linearly spaced along the width of the domain. However, one may choose to have the agents start along the circumference of the field, somewhere within the field, or from a single point. A staggered start time would also vary the flight path recommendations.

The benefits of employing a multi-agent swarm of drones are highlighted in Fig. 7 where a different color indicates each agent's total energy consumed on the stacked bar chart. As the number of agents increases, the time required to map all the sensors decreases. Meanwhile, as the number of drones in the swarm increased, their individual flight path lengths decreased while the total flight path remained relatively consistent for all simulated swarm sizes. The distance traveled can be

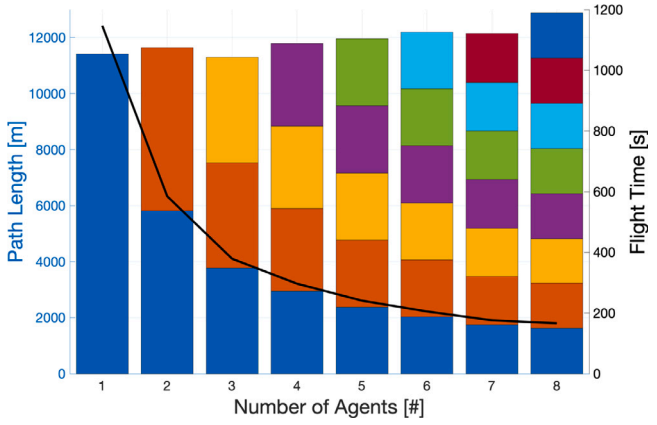

Fig. 7. Split-axis plot showing the total distance traveled (left) and the flight time to read all sensors in a 400 m radius center-pivot irrigation field (right) for swarms of n = 1–8 agents. Each bar in the stacked bar plot shows the distance traveled for each agent.

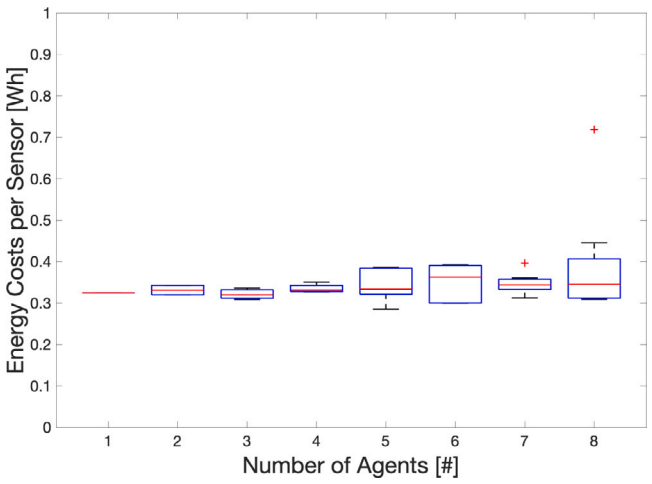

Fig. 8. Box-whisker plot showing the variance of energy consumption per sensor scanned. Low variance indicates the amount of energy spent per target is evenly distributed across all agents. A larger box size corresponds to a larger variance. When five or more agents are simulated, there is a significant imbalance in average energy expenditure per sensor scanned across the drones. This was primarily due to a phenomenon where multiple agents 'race' to scan the same sensor and develop a 'leader–follower' behavior, rendering 'followers' completely ineffective.

correlated with the amount of fuel or battery power a drone consumes, meaning that a swarm of drones uses a comparable amount of energy as a single drone, but performs the scan much faster.

To further analyze the trade-offs in swarm size, the drones' energy expenditure per sensor scanned as a function of swarm size was examined, as shown in Fig. 8. As the number of agents increased, the total average energy consumption per sensor scanned did not significantly change. This agrees with Fig. 7, which shows that the total flight path to scan all of the sensors in the field also did not significantly change when the number of drones was increased. However, the variance of the energy consumption per sensor scanned increased as the number of drones increased. When inspecting the simulations, it was found that this was primarily caused by a scenario where several agents would 'race' to scan the same sensor. Then, once that sensor was scanned and removed from the domain, the same agents would often continue to race one another for subsequent sensors. This 'leader–follower' behavior is wasteful as the agents consume energy, thus creating more conflict between agents instead of collaboration. Four was the optimal number of drones for this scenario because it was the fastest scan that did not demonstrate 'leader–follower' behavior.

The flight paths for a four-agent drone swarm in a 400 m radius center-pivot irrigation field are shown in Fig. 9. Starting from the edge of the simulated domain, the agents traversed through the center-pivot irrigation field and sampled the distributed sensors, as seen in Fig. 9A and B. Initially, the drones seek out the nearest sensors as because they have the strongest interaction force. However, as the flight paths continued to develop (as in Fig. 9C–F) the number of unscanned sensors dwindled, and the relative attraction strength of more distant sensors grew. This continued until the last sensor was scanned, as shown in Fig. 9G, and the drones returned to their initial positions.

Because the flight paths are optimized using a genetic algorithm and the initialization is random, the outcome could theoretically be different every time the simulation is executed, even when the same parameters are used. Table 2, for example, shows the optimal parameters for the top three performing design strings when the four-drone condition was simulated. For parameters such as c_{rep}^{agent}, which is the exponential decay coefficient for the repulsion term emitted by the agent, the 'optimal value' is practically the same for each design string. Meanwhile, for other parameters, such as c_{att}^{sensor}, the value varies by about one-third of the search bounds across the design strings. While it may seem like this indicates that the output is unstable, when the flight paths of the top-performing design strings are simulated, as shown in Fig. 10, it becomes evident that only minor differences exist between the resulting flight paths. This is because genetic algorithms excel at solving highly multivariate problems quickly. Furthermore, the similarities between the top three flight paths indicate the robustness of the solution.

6. Conclusions

For any agricultural field geometry, the proposed SGR algorithm maximizes the coverage of an agricultural field with fewer sensors than a grid-based distribution in most cases. The proposed multi-agent flight path mapping can effectively and efficiently generate flight paths for variable numbers of drones to scan all sensors. Thus, a crop grower could use the algorithms described in this paper to determine the optimal placement of soil sensors inside their own field, the ideal number of drones to sample data from the sensors, and their flight paths. This framework can be adopted for variable-rate irrigation applications to maximize crop yield and minimize environmental pollution.

The aforementioned framework was used to determine the optimal placement of sensors for a 400 m radius center-pivot irrigation field and simulated the flight paths of drone swarms of varying sizes. Four drones provided the best balance between energy efficiency and flight time for the simulated scenario. Using multiple drones also significantly

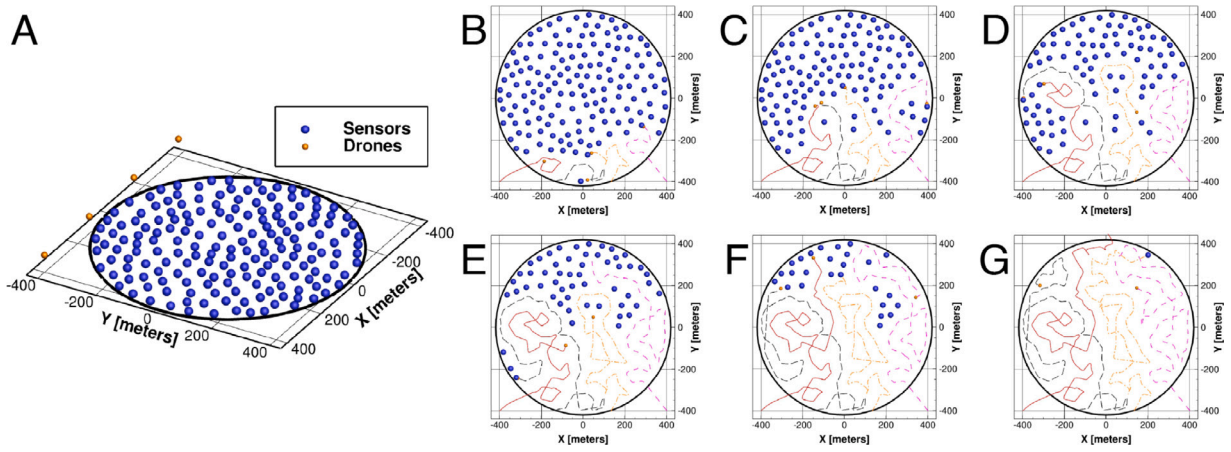

Fig. 9. Sequences of flight paths in a 400 m radius center-pivot irrigation field for a four-agent swarm. (A) Initial configuration of the agents and sensors. (B–G) Development of each agent's flight path throughout simulated time.

Table 2
Optimal parameters for the top three performing design strings for flight paths of four drones.

W_s	W_a	w_{att}^{sensor}	w_{rep}^{sensor}	c_{att}^{sensor}	c_{rep}^{sensor}	w_{att}^{agent}	w_{rep}^{agent}	c_{att}^{agent}	c_{rep}^{agent}
2.38897	6.60861	0.38679	0.34980	0.41784	0.73018	0.28894	0.48590	0.69733	0.32812
2.38633	3.69574	0.36072	0.32646	0.35214	0.78264	0.29032	0.48498	0.72134	0.33702
2.42084	6.98402	0.39193	0.54399	0.69210	0.67569	0.27516	0.48624	0.68220	0.32287

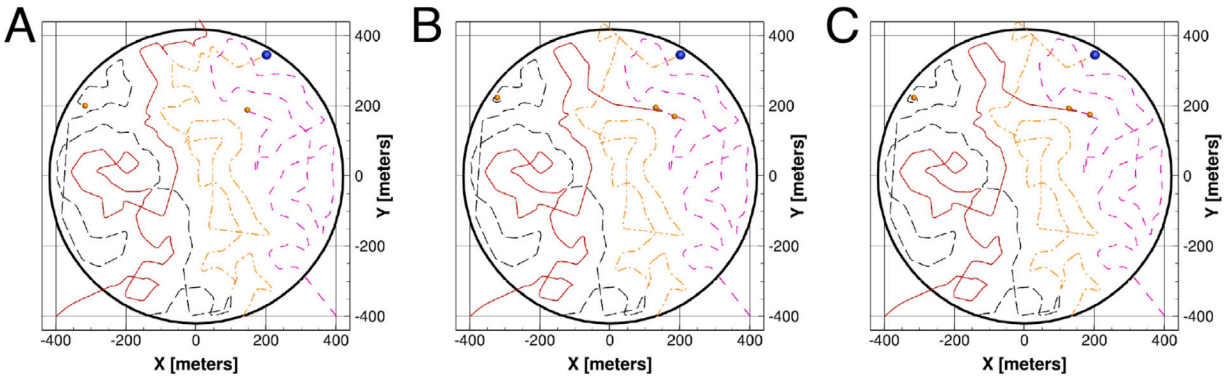

Fig. 10. Flight paths for the top three performing design strings for a four-agent swarm in a 400 m radius center-pivot irrigation field.

decreased the amount of the total time it takes to complete the sensor scanning task within the field compared to a single drone.

The drone flight path mapping shown here does not account for topological features or weather conditions. Further extensions of this framework include adding variations in terrain height and additional outside forces such as wind drag synced with weather data, to obtain a more accurate framework for digital twin capabilities.

Agricultural drone flight path mapping applications are not limited to reading sensors. Recently, drones in precision agriculture have taken a more physical role, such as aerial application of fluids, solids, and biological control agents. In 2015, the Federal Aviation Administration approved the first crop-dusting drone capable of spraying pesticides with tanks weighing more than 55 lbs. This approval allowed the rapid deployment of drones to spray soil amendments and seeds to precise areas indicated by the soil-embedded sensors, reducing the amount of irrigation runoff and seeds dispensed in unwanted areas. The flight path model could also be modified for tasks such as orchard harvesting, where the drone is programmed to collect fruits or nuts from trees and deposit them into boxes.

CRediT authorship contribution statement

Payton Goodrich: Generated the code and figures for the "digital expression of an agricultural field" and "optimized sensor placement" sections, Generated the figures for the "Results and Discussion" section and wrote the manuscript. **Omar Betancourt:** Generated the code and figures for the "flight path mapping" sections, Generated the figures for the "Results and Discussion" section and wrote the manuscript.

Declaration of competing interest

The authors declare that they have no known competing financial interests or personal relationships that could have appeared to influence the work reported in this paper.

Data availability

Data will be made available on request.

Acknowledgments

The drone photography of the farm field shown in Fig. 1D is from the publicly available data set from senseFly. This and similar datasets can be accessed at https://www.sensefly.com/education/datasets/. This work was partially supported by the National Science Foundation Graduate Research Fellowships, USA under Grant No. DGE 1752814, and the Advanced Research Projects Agency - Energy, USA award DE-AR0001013. This work was also partially supported by AFRI Competitive, USA Grant no. 2020-67021-32855/project accession no. 1024262 from the USDA National Institute of Food and Agriculture, USA. This grant is being administered through AIFS: the AI Institute for Next Generation Food Systems. https://aifs.ucdavis.edu.

Appendix A. Supplementary data

Supplementary material related to this article can be found online at https://doi.org/10.1016/j.compag.2022.107591.

References

Ahrens, T., Lobell, D., Ortiz-Monasterio, J., Li, Y., Matson, P., 2010. Narrowing the agronomic yield gap with improved nitrogen use efficiency: a modeling approach. Ecol. Appl. 20 (1), 91–100.

Akbari, Y., Almaadeed, N., Al-maadeed, S., Elharrouss, O., 2021. Applications, databases and open computer vision research from drone videos and images: a survey. Artif. Intell. Rev. 54 (5), 3887–3938.

Akbarzadeh, V., Lévesque, J.-C., Gagné, C., Parizeau, M., 2014. Efficient sensor placement optimization using gradient descent and probabilistic coverage. Sensors 14 (8), 15525–15552.

Anthony, P., Malzer, G., Zhang, M., Sparrow, S., 2012. Soil nitrogen and phosphorus behavior in a long-term fertilization experiment. Agron. J. 104 (5), 1223–1237.

Bachmaier, M., Backes, M., 2008. Variogram or semivariogram? Understanding the variances in a variogram. Precis. Agric. 9 (3), 173–175.

Bertalan, L., Holb, I., Pataki, A., Négyesi, G., Szabó, G., Kupásné Szalóki, A., Szabó, S., 2022. UAV-based multispectral and thermal cameras to predict soil water content – A machine learning approach. Comput. Electron. Agric. 200, 107262. http://dx.doi.org/10.1016/j.compag.2022.107262, URL https://www.sciencedirect.com/science/article/pii/S0168169922005750.

Cao, Q., Cui, Z., Chen, X., Khosla, R., Dao, T.H., Miao, Y., 2012. Quantifying spatial variability of indigenous nitrogen supply for precision nitrogen management in small scale farming. Precis. Agric. 13 (1), 45–61.

Cassman, K.G., Dobermann, A., Walters, D.T., 2002. Agroecosystems, nitrogen-use efficiency, and nitrogen management. AMBIO: J. Human Environ. 31 (2), 132–140.

Chlingaryan, A., Sukkarieh, S., Whelan, B., 2018. Machine learning approaches for crop yield prediction and nitrogen status estimation in precision agriculture: A review. Comput. Electron. Agric. (ISSN: 0168-1699) 151, 61–69. http://dx.doi.org/10.1016/j.compag.2018.05.012, URL https://www.sciencedirect.com/science/article/pii/S0168169917314710.

Comis, D., 2011. Growing crops and saving water in the west. Agric. Res. 59 (7), 12–14.

Dalin, C., Hanasaki, N., Qiu, H., Mauzerall, D.L., Rodriguez-Iturbe, I., 2014. Water resources transfers through Chinese interprovincial and foreign food trade. Proc. Natl. Acad. Sci. 111 (27), 9774–9779.

Deng, F., Zuo, P., Wen, K., Wu, X., 2020. Novel soil environment monitoring system based on RFID sensor and LoRa. Comput. Electron. Agric. 169, 105169. http://dx.doi.org/10.1016/j.compag.2019.105169, URL https://www.sciencedirect.com/science/article/pii/S0168169919319222.

Diacono, M., Rubino, P., Montemurro, F., 2013. Precision nitrogen management of wheat. A review. Agron. Sustain. Dev. 33 (1), 219–241.

Dieter, C.A., 2018. Water Availability and Use Science Program: Estimated Use of Water in the United States in 2015. Geological Survey.

Donev, A., Torquato, S., Stillinger, F.H., 2005a. Neighbor list collision-driven molecular dynamics simulation for nonspherical hard particles. I. Algorithmic details. J. Comput. Phys. 202 (2), 737–764.

Donev, A., Torquato, S., Stillinger, F.H., 2005b. Neighbor list collision-driven molecular dynamics simulation for nonspherical hard particles.: Ii. applications to ellipses and ellipsoids. J. Comput. Phys. 202 (2), 765–793.

Evans, R.G., 2001. Center pivot irrigation. In: Agricultural Systems Research Unit, Vol. 1500. North Plain Agric. Res. Laboratory. USDN-Agric. Res. Service.

Evans, R.G., LaRue, J., Stone, K.C., King, B.A., 2013. Adoption of site-specific variable rate sprinkler irrigation systems. Irrigation Sci. 31 (4), 871–887.

Finger, R., Swinton, S.M., El Benni, N., Walter, A., 2019. Precision farming at the nexus of agricultural production and the environment.

Gellings, C.W., Parmenter, K.E., 2016. Energy efficiency in fertilizer production and use. In: Gellings, C.W. (Ed.), Efficient Use and Conservation of Energy. In: Encyclopedia of Life Support Systems, pp. 123–136.

Gupta, M., Khosla, R., 2012. Precision nitrogen management and global nitrogen use efficiency. In: Proceedings of the 11th International Conference on Precision Agriculture. Indianapolis, Ind, USA.

Hardin, R.G., Barnes, E.M., Delhom, C.D., Wanjura, J.D., Ward, J.K., 2022. Internet of things: Cotton harvesting and processing. Comput. Electron. Agric. 202, 107294. http://dx.doi.org/10.1016/j.compag.2022.107294, URL https://www.sciencedirect.com/science/article/pii/S0168169922006068.

Hedley, C.B., Yule, I.J., 2009. Soil water status mapping and two variable-rate irrigation scenarios. Precis. Agric. 10 (4), 342–355.

Hellerstein, D., Vilorio, D., 2019. Agricultural Resources and Environmental Indicators, 2019. Tech. rep.

Hifi, M., M'hallah, R., 2009. A literature review on circle and sphere packing problems: Models and methodologies. Adv. Oper. Res. 2009.

Hoy, R., 2021. Nebraska summary S1150A for Fendt 1050. Institute of Agriculture and Natural Resources University of Nebraska–Lincoln, URL https://digitalcommons.unl.edu/tractormuseumlit/3481/.

Jourdan, D.B., de Weck, O.L., 2004. Layout optimization for a wireless sensor network using a multi-objective genetic algorithm. In: 2004 IEEE 59th Vehicular Technology Conference. VTC 2004-Spring (IEEE Cat. No. 04CH37514), Vol. 5. IEEE, pp. 2466–2470.

Kanter, D.R., Bell, A.R., McDermid, S.S., 2019. Precision agriculture for Smallholder Nitrogen Management. One Earth 1 (3), 281–284. http://dx.doi.org/10.1016/j.oneear.2019.10.015, URL https://www.sciencedirect.com/science/article/pii/S2590332219301290.

Kerry, R., Oliver, M., Frogbrook, Z., 2010. Sampling in precision agriculture. In: Geostatistical Applications for Precision Agriculture. Springer, pp. 35–63.

Kumar, G.N., Bangi, M., 2018. An extension to winding number and point-in-polygon algorithm. IFAC-PapersOnLine 51 (1), 548–553.

Ladha, J.K., Pathak, H., Krupnik, T.J., Six, J., van Kessel, C., 2005. Efficiency of fertilizer nitrogen in cereal production: retrospects and prospects. Adv. Agron. 87, 85–156.

Lo, T.H., Heeren, D.M., Mateos, L., Luck, J.D., Martin, D.L., Miller, K.A., Barker, J.B., Shaver, T.M., 2017. Field characterization of field capacity and root zone available water capacity for variable rate irrigation. Appl. Eng. Agric. 33 (4), 559–572.

Longchamps, L., Khosla, R., 2017. Precision maize cultivation techniques. In: Achieving Sustainable Cultivation of Maize Volume 2. Burleigh Dodds Science Publishing, pp. 127–157.

Longchamps, L., Khosla, R., Reich, R., Gui, D., 2015. Spatial and temporal variability of soil water content in leveled fields. Soil Sci. Am. J. 79 (5), 1446–1454.

MacDonald, J.M., Korb, P., Hoppe, R.A., 2013. Farm Size and the Organization of US Crop Farming. Tech. rep.

Metropolis, N., Rosenbluth, A.W., Rosenbluth, M.N., Teller, A.H., Teller, E., 1953. Equation of state calculations by fast computing machines. J. Chem. Phys. 21 (6), 1087–1092.

Mueller, M.W., Hehn, M., D'Andrea, R., 2015. A computationally efficient motion primitive for quadrocopter trajectory generation. IEEE Trans. Robot. 31 (6), 1294–1310.

Patrício, D.I., Rieder, R., 2018. Computer vision and artificial intelligence in precision agriculture for grain crops: A systematic review. Comput. Electron. Agric. 153, 69–81.

Pereira, F.S., de Lima, J., Freitas, R., Dos Reis, A., Amaral, L., Figueiredo, G., Lamparelli, R., Magalhães, P., 2022. Nitrogen variability assessment of pasture fields under an integrated crop-livestock system using UAV, PlanetScope, and Sentinel-2 data. Comput. Electron. Agric. 193, 106645. http://dx.doi.org/10.1016/j.compag.2021.106645, URL https://www.sciencedirect.com/science/article/pii/S0168169921006621.

Ritchie, H., Roser, M., 2020. CO_2 and Greenhouse Gas Emissions. Our World in Data, https://ourworldindata.org/co2-and-other-greenhouse-gas-emissions.

Robert, P.C., Rust, R.H., Larson, W.E., 1995. Proceedings of site-specific management for agricultural systems: second international conference, march 27-30, 1994 thunderbird hotel, 2201 east 78th st., minneapolis, MN: conducted by the department of soil science and minnesota extension service, university of minnesota. In: 2nd International Conference on Site-Specific Management for Agricultural Systems., Minneapolis, Minn.(USA), 1994. American Society of Agronomy.

Robertson, G.P., Klingensmith, K.M., Klug, M.J., Paul, E.A., Crum, J.R., Ellis, B.G., 1997. Soil resources, microbial activity, and primary production across an agricultural ecosystem. Ecol. Appl. 7 (1), 158–170.

Sela, S., Woodbury, P., Van Es, H., 2018. Dynamic model-based N management reduces surplus nitrogen and improves the environmental performance of corn production. Environ. Res. Lett. 13 (5), 054010.

Shahandeh, H., Wright, A., Hons, F., Lascano, R., 2005. Spatial and temporal variation of soil nitrogen parameters related to soil texture and corn yield. Agron. J. 97 (3), 772–782.

Sørensen, L.Y., Jacobsen, L.T., Hansen, J.P., 2017. Low cost and flexible UAV deployment of sensors. Sensors 17 (1), 154.

Steinhaus, H., 1999. Mathematical Snapshots. Courier Corporation.

SU, S.L., Singh, D., Baghini, M.S., 2014. A critical review of soil moisture measurement. Measurement 54, 92–105.

Sun, X., Fang, W., Gao, C., Fu, L., Majeed, Y., Liu, X., Gao, F., Yang, R., Li, R., 2022. Remote estimation of grafted apple tree trunk diameter in modern orchard with RGB and point cloud based on SOLOv2. Comput. Electron. Agric. 199, 107209. http://dx.doi.org/10.1016/j.compag.2022.107209, URL https://www.sciencedirect.com/science/article/pii/S0168169922005245.

TOMBE, R., 2020. Computer vision for smart farming and sustainable agriculture. In: 2020 IST-Africa Conference (IST-Africa). IEEE, pp. 1–8.

Tosato, P., Facinelli, D., Prada, M., Gemma, L., Rossi, M., Brunelli, D., 2019. An autonomous swarm of drones for industrial gas sensing applications. In: 2019 IEEE 20th International Symposium on" a World of Wireless, Mobile and Multimedia Networks"(WoWMoM). IEEE, pp. 1–6.

Widom, B., 1966. Random sequential addition of hard spheres to a volume. J. Chem. Phys. 44 (10), 3888–3894.

Zohdi, T., 2019. The Game of Drones: rapid agent-based machine-learning models for multi-UAV path planning. Comput. Mech. 65, 217–228.

Zohdi, T., 2021a. A digital-twin and machine-learning framework for the design of multiobjective agrophotovoltaic solar farms. Comput. Mech. 68 (2), 357–370.

Zohdi, T., 2021b. A digital-twin and machine-learning framework for ventilation system optimization for capturing infectious disease respiratory emissions. Arch. Comput. Methods Eng. 28 (6), 4317–4329.

Zohdi, T., 2022. A digital-twin and machine-learning framework for precise heat and energy management of data-centers. Comput. Mech. 1–16.